Measurement Science
and Technology

PURPOSE-LED
PUBLISHING™

PAPER • **OPEN ACCESS**

A geometric principle for absolute angular measurement using single-point ToF ranging

To cite this article: Ertugrul Cetinsoy 2026 *Meas. Sci. Technol.* **37** 455101

View the article online for updates and enhancements.

You may also like

- Depth-guided selective cross-modal fusion network for deep-sea polymetallic nodule segmentation
Heqing Qin, Jianfeng Liang, Xuerong Cui et al.
- DGIM-SAM: dual-kernel gated interaction modulation and spectral adaptive modulation for real-time wildfire detection
Dan Shan, Yanfeng Li and Dongming Liu
- A cross-condition fault diagnosis method for rolling bearings combining content-conditioned positional encoding and label-conditioned in-context learning
Nengchao Wu, Shengcai Wang, Junjie Bao et al.



This content was downloaded from IP address 193.255.177.234 on 15/11/2026 at 18:25

Measurement Science and Technology

Check for updates

OPEN ACCESS

RECEIVED
6 July 2026

REVISED
19 October 2026

ACCEPTED FOR PUBLICATION
27 October 2026

PUBLISHED
9 November 2026

Original content from this work may be used under the terms of the Creative Commons Attribution 4.0 licence.

Any further distribution of this work must maintain attribution to the author(s) and the title of the work, journal citation and DOI.

PAPER

A geometric principle for absolute angular measurement using single-point ToF ranging

Ertugrul Cetinsoy*

Faculty of Technology, Marmara University, Istanbul, Türkiye
* Author to whom any correspondence should be addressed.

E-mail: ertugrul.cetinsoy@marmara.edu.tr

Keywords: absolute angular measurement, experimental measurement validation, geometric encoding, optical metrology, time-of-flight LiDAR

Abstract

Absolute angular position measurement is critical for automated systems, yet conventional optical and magnetic encoders often suffer from complex alignment, vulnerability to dirty environments, or high cost. This paper proposes a proof-of-concept angular measurement scheme that converts rotational displacement into monotonic distance variations via a helical reference surface, measured by a single-point time-of-flight distance sensor. A theoretical model incorporating a reference distance and monotonic mapping bounds is formulated to establish the one-to-one angular transformation within a 350° interval. To suppress impulsive distance outliers caused by surface reflections and optical transitions, a threshold-based temporal consistency filter is applied. Experimental validation using a VL53L1X-based prototype demonstrates the fundamental feasibility of the approach, achieving degree-level accuracy under controlled in-air and shallow submerged conditions (10 cm depth). Dynamic evaluations across various rotational speeds, direction reversals, and transient regimes highlight both the capabilities and operational limits of the system, particularly regarding filter-induced latency and sample rejection during rapid motion. Rather than competing with high-precision commercial encoders, the proposed method serves as a simple, low-cost feasibility study tailored for moderate-accuracy applications where environmental tolerance and mechanical simplicity are prioritized.

1. Introduction

Absolute angular position measurement is a fundamental requirement in robotics, industrial automation and autonomous systems [1–3]. Traditional angular sensing approaches predominantly rely on optical, magnetic, inductive, or capacitive encoders [4–7]. Among these, optical encoders represent the benchmark for high-precision applications, achieving sub-degree or arcsecond-level resolutions through finely patterned code discs and optoelectronic receiver arrays [4, 8, 9]. Magnetic encoders, utilizing Hall-effect or magnetoresistive sensors, offer robust alternatives that are less sensitive to dust, oil, and fluid contamination compared to their optical counterparts [5, 10, 11]. However, these conventional high-precision technologies typically require stringent mechanical alignment, specialized signal-conditioning electronics, and strict structural encapsulation to maintain reliable absolute positioning [6, 7, 12].

Despite their superior precision, commercial absolute encoders often present operational constraints in cost-sensitive, space-constrained, or environmentally harsh applications [8, 13]. Optical encoders are notoriously susceptible to lens contamination, condensation, and mechanical shock, where foreign particles or moisture ingress can disrupt the light path and degrade measurement integrity [4, 9, 14]. Magnetic encoders, while resilient to optical obstructions, remain vulnerable to strong external electromagnetic interference (EMI) and stray magnetic fields commonly generated by high-power motors or actuators [5, 11]. Furthermore, both technologies generally rely on multi-channel or multi-track sensing elements, which inherently increases system complexity, manufacturing overhead, and assembly alignment tolerances [12, 15].

© 2026 The Author(s). Published by IOP Publishing Ltd

To mitigate these constraints, alternative non-contact angular sensing schemes utilizing geometric target transformations paired with single-point distance transducers have gained research interest [13, 16]. By mapping rotational displacement into a physical distance variation, a single-point sensor can reconstruct the absolute angular orientation of a shaft [16, 17]. Time-of-flight (ToF) distance sensors, particularly those based on solid-state vertical-cavity surface-emitting lasers (VCSEL) and single-photon avalanche diodes (SPAD), have emerged as compact, low-cost, and digitally integrated candidates for distance measurement [14, 18]. Unlike complex multi-sensor arrays, single-point ToF sensors offer low component counts and straightforward digital interfaces, making them attractive for minimal-complexity sensing architectures [15, 18].

However, adapting single-point ToF sensors for absolute angular measurement introduces unique physical and signal processing trade-offs. The achievable angular resolution is inherently constrained by the intrinsic ranging precision and beam spot size of the ToF transducer, yielding degree-level rather than sub-degree performance [16, 17]. Additionally, optical transitions at target geometric discontinuities can trigger transient ranging anomalies and impulsive outliers [17, 18]. While existing literature focuses heavily on high-precision solutions through complex multi-component encoders [4–9], a clear gap remains in systematically evaluating minimal-complexity, single-sensor architectures tailored for moderate-accuracy applications where mechanical simplicity, low cost, and environmental tolerance are prioritized over arcsecond-level precision.

Motivated by this concept, this work presents a proof-of-concept investigation into a continuous geometric encoding principle, where shaft angular position is mapped into a continuous monotonic distance using a helical reference surface and recovered by a single-point ToF distance sensor. Within a defined monotonic interval that is bounded by a reference baseline distance and a geometric dead-zone, the proposed architecture establishes a continuous mapping using only a single ranging channel. Rather than targeting sub-arcsecond precision, this work addresses a complementary class of applications in which mechanical simplicity, environmental robustness and ease of integration are of greater practical importance than maximum achievable resolution.

To evaluate the proposed concept, a proof-of-concept prototype based on a low-cost VL53L1X ToF sensor was constructed and experimentally validated under both in-air and shallow submerged conditions (10 cm depth). A computationally efficient threshold-based temporal consistency filtering was employed to suppress impulsive ranging outliers, and the resulting performance was evaluated in terms of accuracy, outlier rejection rates, and dynamic limits. Beyond demonstrating experimental feasibility, the study establishes the relationship between geometric sensitivity and ranging resolution, while outlining a geometry-aware continuity restoration strategy to address the helical transition zone during full-revolution operation.

The primary contributions of this work are:

1. Formulation of a revised angular mapping model incorporating a baseline distance offset (d_0) to formally define the monotonic interval, dead-zone region, and one-to-one mapping bounds.
2. Implementation and empirical characterization of a temporal consistency filter, quantifying sample rejection rates, filter-induced latency, and signal-hold behavior during dynamic motion.
3. Experimental validation of the proof-of-concept prototype across variable speeds, direction reversals, and shallow submerged conditions (10 cm depth) to establish clear operational boundaries for moderate-accuracy sensing.

The remainder of this paper is organized as follows. Section 2 presents the operating principle and geometric model of the proposed measurement approach. Section 3 describes the experimental methodology and validation procedure. Section 4 presents experimental results together with uncertainty analysis, dead-zone compensation, dynamic measurement considerations and practical implementation aspects. Section 5 summarizes the principal findings and outlines directions for future research.

2. Continuous geometric encoding principle

The proposed measurement approach is based on the premise that absolute angular position can be encoded by a continuous geometric quantity rather than by discrete spatial codes. Instead of assigning binary patterns to specific angular intervals, this method establishes a continuous physical relationship between the angular position of a rotating shaft and the distance measured by a single-point ToF sensor.

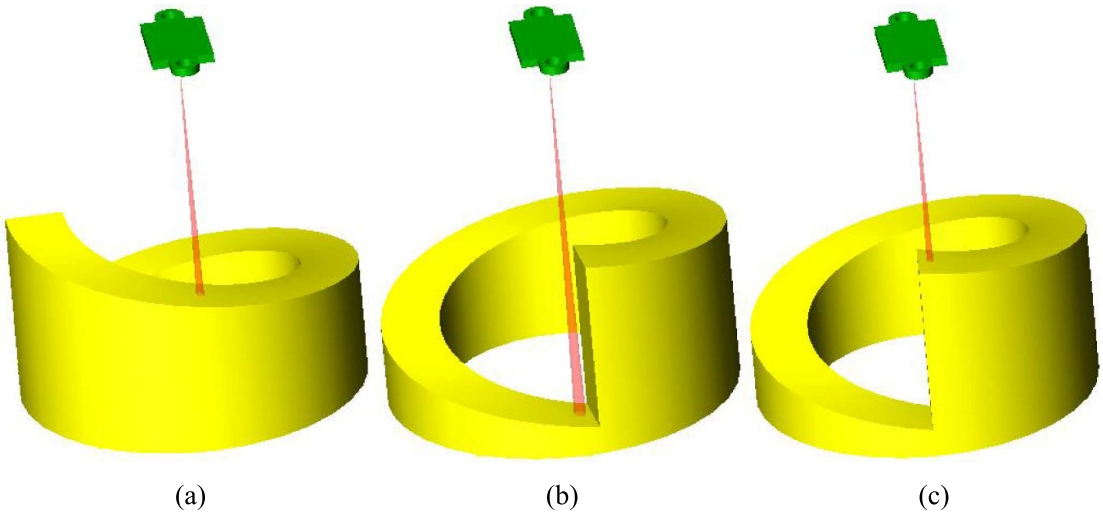

Figure 1. Helical implementation of the proposed continuous geometric encoding principle showing the variation of the sensor-to-surface distance with shaft rotation.

Consequently, the angular coordinate is recovered directly from a single optical distance channel without requiring multi-track code discs or complex receiver arrays.

For absolute position measurement, the transformed geometric profile must satisfy two fundamental conditions:

1. The distance function must vary monotonically with angular position over the primary operating interval.
2. Each angular position within this interval must correspond to a unique distance value, thereby establishing a one-to-one mapping between the shaft angle and the measured range.

These requirements are realized by shaping the rotating reference surface such that its distance from the stationary ToF sensor varies continuously with angular position. Two alternative target topologies can implement this principle:

- **Helical configuration (axial ranging):** The target forms an axial helical ramp where the measured distance along the axis of rotation varies continuously over one full revolution (figure 1).
- **Spiral configuration (radial ranging):** The target geometry forms a radial spiral profile where the radial distance from the center of rotation changes monotonically with angle (figure 2).

Although both configurations embody the same continuous geometric encoding principle, the helical design was selected for experimental validation due to its straightforward mechanical alignment, direct axial line-of-sight integration, and simpler manufacturing tolerances.

2.1. Theoretical mapping model

In the helical configuration, the shaft angular position θ is mapped into a continuous axial displacement measured by the ToF sensor. For an ideal helical target with a constant pitch, the continuous distance-to-angle relationship within the monotonic measurement interval is formulated as:

$$\theta = \frac{360^\circ}{P}(d - d_o) \tag{1}$$

where:

- d is the instantaneous distance reported by the ToF sensor,
- d_0 represents the baseline reference distance corresponding to the minimum physical clearance between the ToF sensor window and the highest point of the helical surface at $\theta = 0^\circ$,
- P is the total axial pitch height of the helical surface corresponding to one full 360° rotation.

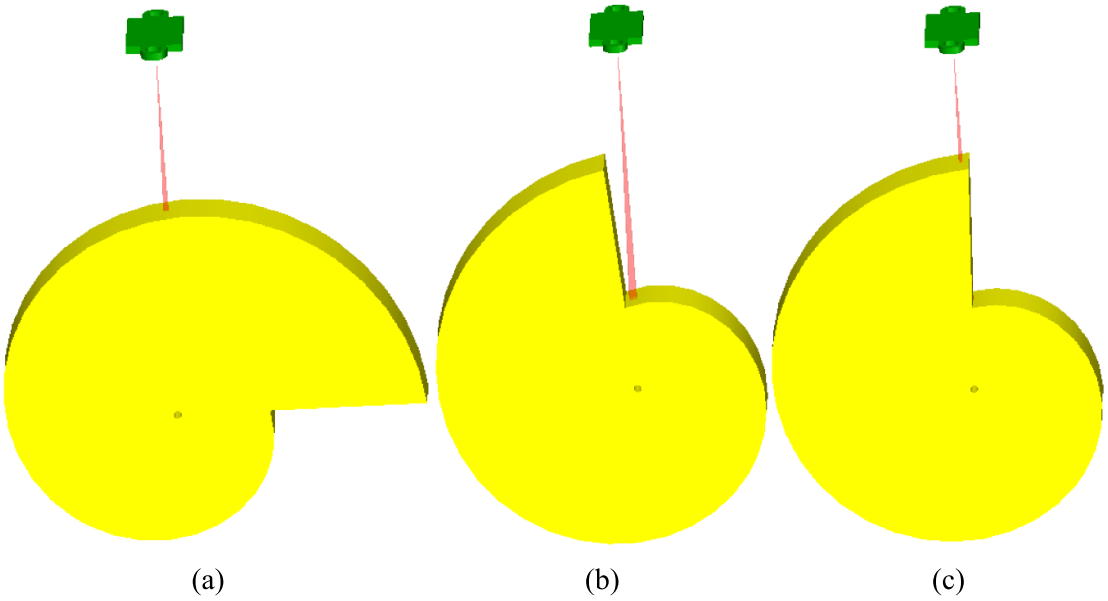

Figure 2. Front view of the spiral type of the proposed encoder with a variety of shaft positions.

Equation (1) can be expressed in a linear calibration form:

$$\theta = a \cdot d + b \tag{2}$$

where $a = \frac{360^\circ}{P}$ is the geometric transformation gain ($^\circ \mathrm{mm}^{-1}$), and $b = -\frac{360^\circ}{P} d_0$ represents the static calibration offset incorporating sensor-to-target mechanical positioning.

2.2. Operational boundaries and one-to-one mapping conditions

To guarantee a deterministic, one-to-one inverse mapping from distance d back to angle θ, the measurement domain must strictly comply with the following physical and geometric boundaries:

1. Valid distance domain: The measured distance d varies strictly within the interval $d \in [d_{\min}, d_{\max}]$ where $d_{\min} = d_0$ and $d_{\max} = d_0 + P$.
2. Valid angular domain: The recoverable angular coordinate spans $0^\circ \leq \theta < 360^\circ - \Delta\theta_{\mathrm{dz}}$, where $\Delta\theta_{\mathrm{dz}}$ denotes the angular width of the geometric transition region.
3. Transition dead-zone region ($\Delta\theta_{\mathrm{dz}}$): At the angular boundary ($\theta \to 360^\circ$), the helical ramp terminates and steps down vertically back to $\theta = 0^\circ$. Within this step-transition region ($\Delta\theta_{\mathrm{dz}}$), the finite optical spot size of the ToF laser beam simultaneously illuminates both the upper ($\theta \approx 0^\circ$) and lower ($\theta \approx 350^\circ$) surfaces of the target. This optical superposition breaks the assumption of single-point distance measurement, causing transient ranging anomalies and outlier spikes.

Consequently, the continuous one-to-one inverse mapping is strictly valid within the monotonic region ($0^\circ \leq \theta < 360^\circ - \Delta\theta_{\mathrm{dz}}$), whereas data sampled within the transition dead-zone requires dedicated temporal filtering and continuity restoration routines during full-revolution dynamic operations.

3. Experimental methodology

3.1. Measurement system

A proof-of-concept measurement system was developed to experimentally validate the proposed continuous geometric encoding principle. The prototype employed a helical reference surface manufactured from acrylonitrile butadiene styrene (ABS) using fused deposition modeling (FDM) additive manufacturing. The helical structure had an outer diameter of 300 mm, a ramp width of 40 mm and a pitch of $P = 200\mathrm{mm/rev}$, the latter being bounded by the available build volume of the 3D printer (figure 3).

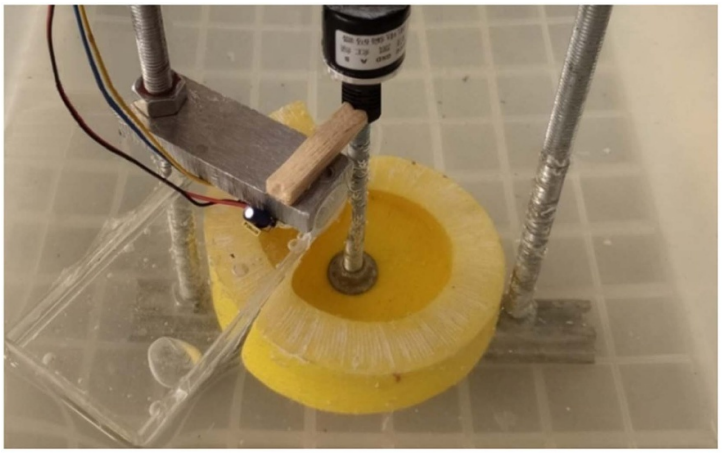

Figure 3. Test setup for the validation of the proposed sensor with helical gear submerged in water.

The helical reference was rigidly mounted on the shaft of a commercial H38S400B quadrature encoder providing an angular resolution of 0.225° (1600 CPR). The quadrature encoder served exclusively as the ground truth reference measurement system for performance verification and was not involved in the estimation process.

Axial distance measurements were acquired using a VL53L1X single-point ToF sensor positioned above the helical surface with a nominal baseline clearance of $d_0 \approx 300$ mm corresponding to $\theta = 0°$. Operating via a 940 nm VCSEL emitter with a field of view of approximately 5°, the sensor projects an optical spot diameter of $S_d \approx 22.7$ mm onto the helical ramp at the baseline clearance d_0. This finite spot footprint defines the spatial boundary of the geometric step transition ($\Delta\theta_{dz}$) described in section 2.2.

According to the manufacturer specifications, the sensor provides a measurement range between 40 mm and 4000 mm with a nominal ranging resolution of 1 mm. For the selected helical pitch of $P = 200\text{mm/rev}$, this corresponds to a geometric sensitivity of $a = 360°/P = 1.8°\text{mm}^{-1}$ of measured distance. Consequently, the achievable angular resolution of the prototype is fundamentally limited by the combined sensor resolution and geometric sensitivity rather than by the estimation algorithm itself. The selected geometry was therefore intended to experimentally validate the theoretical relationship presented in section 2 using a low-cost ToF sensor, rather than to maximize absolute angular precision.

Both the ToF sensor and the reference encoder were interfaced with an STM32F401 microcontroller. Distance measurements were acquired via the I^2C bus at a sampling frequency of $f_s \approx 50$ Hz, while the quadrature encoder pulses were decoded using hardware timer peripherals. All measurement data were transmitted to a host computer through an RS232 serial connection for offline analysis and performance evaluation.

3.2. Calibration procedure

Although the proposed measurement principle establishes a deterministic relationship between angular position and measured distance, practical implementation introduces systematic deviations arising from mechanical assembly tolerances, sensor alignment and 3D-printing surface inaccuracies of the helical surface. Therefore, a linear calibration procedure was performed prior to performance evaluation to identify the experimental parameters of the theoretical model derived in section 2.

The reference encoder provided the ground-truth angular position (θ_{ref}), while the corresponding ToF distance measurements (d) were recorded throughout the valid monotonic range ($0° \leq \theta < 360° - \Delta\theta_{dz}$). A least-squares linear regression was then applied to identify the calibration coefficients a_{cal} and b_{cal},

$$\theta = a_{cal} \cdot d + b_{cal} \tag{3}$$

where a_{cal} represents the empirical distance-to-angle conversion gain (°/mm) and b_{cal} compensates for the physical baseline clearance (d_0) and static sensor offset errors. The calibrated model was subsequently applied to all experimental measurements presented in this work.

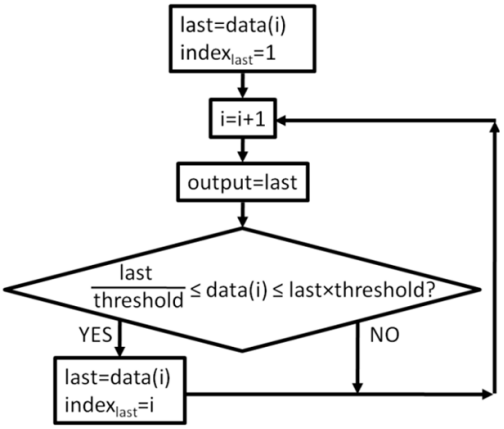

Figure 4. Algorithm schematic of threshold-based temporal consistency filter.

During submerged operation, the propagation velocity of light decreases due to the refractive index of water ($n \approx 1.33$). Accordingly, the calibration coefficients were independently identified for underwater measurements to compensate for the modified optical scaling.

3.3. Experimental protocol

The proposed measurement principle was evaluated under two different environments to investigate its performance and robustness against changes in the optical propagation medium.

In the first experiment, measurements were performed under normal atmospheric conditions to establish the baseline performance of the system. In the second experiment, the helical encoder assembly was tested under shallow submerged conditions at a water depth of approximately 10 cm. The optical window of the ToF sensor was positioned slightly below the water surface to eliminate refraction at the air-water interface, whereas the electronic circuitry remained above the water level to ensure safe operation (figure 3).

To evaluate both steady-state and dynamic response, tests were conducted at a baseline rotational speed of 30 RPM, representing typical operating speeds of robotic joints and grippers, as well as under variable speed profiles 14.7 RPM to 100 RPM and direction reversals to evaluate system latency, tracking limits, and dynamic robustness.

3.4. Signal processing and outlier suppression

Raw distance measurements obtained from the VL53L1X sensor exhibited occasional high-amplitude impulsive outliers originating from stochastic ToF ranging noise and transient optical scattering across the helical step discontinuity ($\Delta\theta_{\mathrm{dz}}$). To maintain low computational complexity suitable for resource-constrained embedded microcontrollers, a threshold-based temporal consistency filter was implemented.

It is important to emphasize that this filtering mechanism is designed solely for impulsive outlier suppression across step transitions rather than for intrinsic sensor resolution enhancement or noise smoothing. The filter evaluates the temporal rate-of-change between consecutive distance readings. A raw sample $d(k)$ is accepted if the inter-sample difference satisfies a maximum threshold percentage criterion relative to the previously accepted value $d(k-1)$:

$$\left|\frac{d(k)-d(k-1)}{d(k-1)}\right| \leq \Delta d_{\max}. \tag{4}$$

Measurements satisfying equation (5) are updated immediately, whereas outlying samples falling within the transition dead-zone are discarded and temporarily held at the last valid state $d(k-1)$ (figure 4).

To prevent filter lock-up, a maximum hold limit of $N_{\mathrm{hold}_{\max}} = 4$ consecutive samples is enforced. The percentage thresholds were optimized experimentally by minimizing false outlier detections while maximizing step-jump rejection, yielding optimal threshold ratios of 80% for in-air operations and 25% for shallow submerged operations.

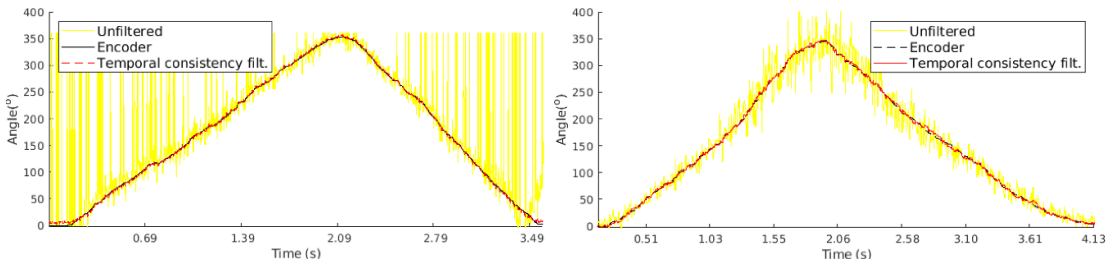

Figure 5. Raw angular position estimation and performance of threshold-based temporal consistency filter for air (a) and water (b).

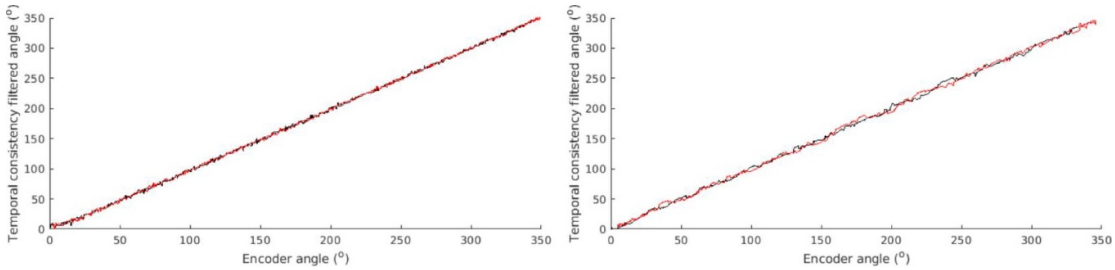

Figure 6. Temporal consistency filter output vs ground-truth encoder measurements for air (a) and water (b).

3.5. Performance evaluation

The performance of the proposed measurement principle was quantified by comparing the estimated angular position (θ) with the ground-truth reference encoder measurements (θ_{ref}). Quantitative evaluation was based on the RMSE, mean bias error, standard deviation, maximum absolute error and measurement repeatability.

Measurement repeatability was assessed by acquiring $N \geq 10$ repeated revolutions at identical angular positions under steady-state rotation. For each angular sample position, the sample mean ($\overline{\theta}$), standard deviation (s), and the repeatability interval (R_{95}) corresponding to a 95% confidence level ($k = 2$) were calculated using equations (5)–(7),

$$\overline{\theta} = \frac{1}{N}\sum_{i=1}^{N}\theta_i \tag{5}$$

$$s = \sqrt{\frac{\sum_{i=1}^{N}\left(\theta_i - \overline{\theta}\right)^2}{N-1}} \tag{6}$$

$$R_{95} = \pm 2\text{s}. \tag{7}$$

These statistical metrics provide a comprehensive evaluation of both measurement accuracy, precision, and operational repeatability for the proposed geometric encoding approach.

4. Results and discussion

4.1. Static atmospheric and submerged measurement performance

The proposed continuous geometric encoding principle was first evaluated under steady-state operating conditions by comparing the angular position estimated from the single-point ToF sensor with the reference quadrature encoder. Figure 5 presents a comparison of the raw angular estimates obtained directly after calibration and threshold-based temporal consistency filter outputs with the reference measurements, while figure 6 demonstrates the insignificant hysteresis behavior of the filtered estimates. The corresponding statistical performance metrics are summarized in table 1.

Table 1. Statistical performance of angular position estimation in air and water media.

Metric	Air (Raw)	Air (Filtered)	Water (Raw)	Water (Filtered)
Number of samples, N	2571	2571	1605	1605
RMSE	83.38°	1.85°	20.01°	2.10°
Standard deviation (s)	79.33°	1.82°	19.99°	2.04°
Mean error (bias, $\bar{e}$)	25.70°	−0.04°	1.02°	0.13°
Maximum absolute error	359.00°	9.24°	86.43°	8.19°
Mean absolute error (MAE)	—	1.44°	—	1.56°
Minimum error	−126.46°	−8.24°	−86.43°	−6.44°
Maximum error	359.00°	8.32°	86.43°	8.19°
Repeatability (R_{95})	—	±3.70°	—	±4.20°
95% confidence interval of mean	—	±0.095°	—	±0.14°

The raw, unfiltered measurements exhibited severe deviations from the reference angle in both media. These deviations were dominated by sporadic, high-amplitude impulsive outliers rather than continuous measurement noise. In air, these spikes reached the full physical span (359.00°), leading to an unacceptably high RMSE of 83.38°. In water, the raw RMSE was 20.01°.

Upon applying the threshold-based temporal consistency filter, the estimated angular position closely tracked the reference encoder throughout the entire monotonic range ($0° \leq \theta < 360° - \Delta\theta_{dz}$). The RMSE dropped drastically to 1.85° in air and 2.10° in water, representing an error reduction exceeding 97% and 89%, respectively. The residual mean bias remained virtually zero (−0.04° in air and 0.13° in water), confirming that the temporal consistency filtering mechanism effectively rejects impulsive outliers without introducing systematic phase distortion or scale attenuation.

Repeatability was evaluated using $N \geq 10$ consecutive steady-state revolutions. The 95% confidence repeatability interval ($R_{95} = \pm 2s$) yielded ±3.70° in air and ±4.20° in water. These results demonstrate that the continuous geometric transformation provides a highly stable and repeatable mapping once transient optical anomalies are suppressed.

4.2. Noise characteristics and temporal consistency filtering

The raw ToF measurement noise does not follow a standard zero-mean Gaussian distribution. Instead, it is characterized by a heavy-tailed, non-Gaussian distribution caused by stochastic optical transit failures, specular surface reflections, and edge-scattering phenomena near the helical step transition ($\Delta\theta_{dz}$). These optical anomalies produce severe, high-amplitude impulsive outliers rather than small continuous Gaussian fluctuations. Traditional linear low-pass or moving-average filters are inherently unsuitable for such noise; they smear impulsive outliers across multiple samples, distorting valid angular trends and introducing dynamic phase lag.

To suppress these high-amplitude optical spikes without smoothing out continuous physical motion, the threshold-based temporal consistency filter introduced in section 3.4 (equation (4)) evaluates the inter-sample change rate relative to the previous valid state. Because the optical noise spikes are an order of magnitude larger than the maximum possible physical distance increment between consecutive samples within the intended operational envelope ($\omega \leq$ 100 RPM), the filter easily discriminates between valid shaft rotation and sensor glare.

To evaluate the stability of this filtering mechanism during dynamic shaft rotation, sample rejection rates were evaluated across rotational speeds ranging from 14.7 RPM up to the system's target operational boundary of 100 RPM. The sample rejection rate $R_{reject}$is defined as:

$$R_{\text{reject}} = \left(\frac{N_{\text{rejected}}}{N_{\text{total}}} \right) \times 100\%. \tag{8}$$

Across the entire evaluated operating range ($\omega \leq 100$ RPM) the sample rejection rate remained virtually independent of rotational speed, stabilizing at $R_{\text{reject}} \approx 4.0\% - 5.2\%$. Figure 7 illustrates the distribution of the number of consecutively rejected samples under both in-air and submerged conditions. The majority of rejection events are concentrated at lower consecutive counts, strictly capped at a maximum of $N_{\text{hold}_{\text{max}}} = 4$ consecutive samples, leading to a sample-hold latency upper bound of $\tau_{\text{filter}_{\text{max}}} = 4\tau_s = 80$ ms.

Based on experimental results, the average algorithmic latency introduced by sample holds in the temporal consistency filter is approximately $\overline{\tau}_{\text{filter}} \approx 0.1\tau_s = 2$ ms where $\tau_s = 20$ ms. At the maximum

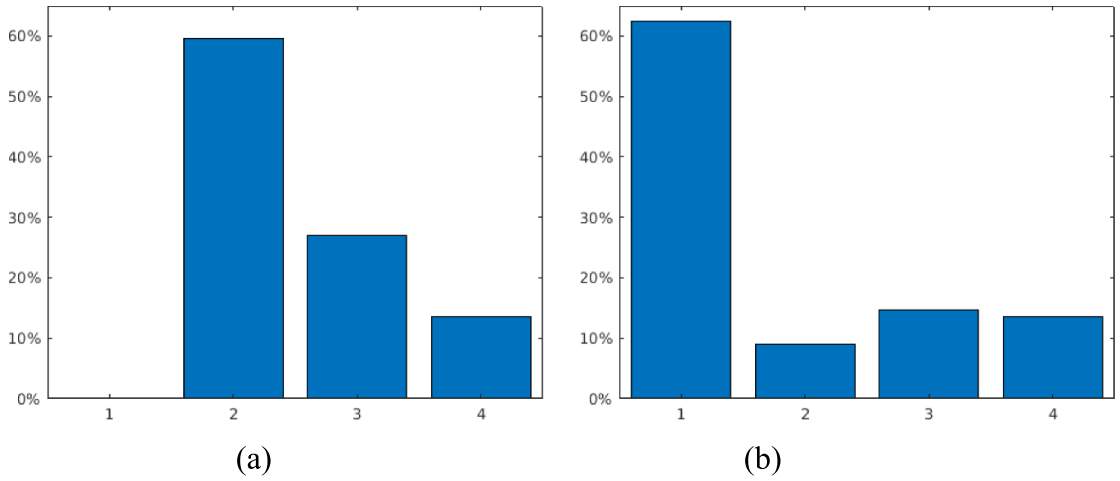

Figure 7. Distribution of number of consecutively rejected samples under in-air (a) and submerged (b) conditions.

target speed of $\omega = 100$ RPM $(600°/s)$, this average algorithmic latency induces a mean dynamic tracking offset bounded by 1.2°. Furthermore, at this maximum operating speed, the physical angular displacement between consecutive samples at $f_s = 50$ Hz is $\Delta\theta = 12.0°$. Because this true physical variation remains well below the strict outlier threshold designed for high-amplitude glare rejection, no valid motion data is misclassified, and no artificial sample-hold steps are introduced by shaft rotation. These results confirm that for applications within $\omega \leq 100$ RPM, such as robotic joint monitoring, valve positioning, and industrial actuators, the temporal consistency filter provides robust, speed-invariant optical noise rejection at an average filter-originated tracking error of 1.2°.

4.3. Combined standard measurement uncertainty analysis (GUM framework)

To rigorously evaluate the metrological performance and establish a complete uncertainty budget in accordance with the ISO/IEC guide to the expression of uncertainty in measurement (GUM), the functional measurement model is expressed as:

$$\theta = f(d, P, d_0) = \frac{360°}{P}(d - d_0) + \delta\theta_{\text{mech}} + \delta\theta_{\text{surf}} \tag{9}$$

where d is the measured ToF distance, $P = 200$ mm is the helical pitch, $d_0 = 300$ mm is the baseline distance, $\delta\theta_{\text{mech}}$ represents combined mechanical assembly errors such as shaft eccentricity and radial runout, and $\delta\theta_{\text{surf}}$ accounts for surface roughness and FDM manufacturing tolerances.

The standard uncertainties associated with each input quantity are categorized into evaluations based on statistical analysis of series of observations (Type A) and evaluations based on prior knowledge, manufacturer specifications or geometric tolerances (Type B):

1. ToF distance sensor quantization and precision (u_d): The VL53L1X sensor has a nominal distance resolution of $\Delta d = 1.0$ mm with a rectangular probability distribution. Its Type B standard uncertainty is:

$$u_d = \frac{\Delta d}{\sqrt{3}} = \frac{1.0}{\sqrt{3}} \approx 0.577 \text{ mm}. \tag{10}$$

With a geometric sensitivity of $c_d = \frac{\partial\theta}{\partial d} = \frac{360°}{P} = 1.8°/mm$, the angular uncertainty contribution is $u_1 = c_d \cdot u_d = 1.039°$.

2. Helical pitch manufacturing tolerance (u_P): The FDM 3D printer build volume and slicing accuracy yield a pitch variation of $\Delta P = \pm 0.5$ mm over $P = 200$ mm/rev. Assuming a triangular distribution:

$$u_P = \frac{0.5}{\sqrt{6}} \approx 0.204 \text{ mm}. \tag{11}$$

The sensitivity coefficient is $c_P = \frac{\partial\theta}{\partial P} = -\frac{360°}{P^2}(d - d_0)$. When evaluated at mid-span ($d - d_0 = 100$ mm $\Longleftrightarrow$ $\theta = 180°$), $c_P = -0.9°/\text{mm}$ gives $u_2 = |c_P| \cdot u_P = 0.184°$.

Table 2. GUM uncertainty budget for absolute angular measurement in air.

Uncertainty Source x_i	Value Δx_i	Probability distribution	Standard uncertainty $u(x_i)$	Sensitivity coefficient c_i	Uncertainty contribution $u_i(\theta)$	Variance contribution(%)
ToF sensor resolution (d)	1.0 mm	Rectangular	0.577 mm	$1.80^\circ/mm$	1.039°	88.9%
Baseline clearance (Δd_0)	0.3 mm	Rectangular	0.173 mm	$-1.80^\circ/mm$	0.312°	8.0%
Helical pitch (P)	0.5 mm	Triangular	0.204 mm	$-0.90^\circ/mm$	0.184°	2.8%
Shaft eccentricity (e_r)	0.15 mm	U-shaped	0.023 mm	$1.80^\circ/mm$	0.041°	0.1%
Surface roughness (R_z)	0.022 mm	Rectangular	0.013 mm	$1.80^\circ/mm$	0.023°	0.04%
Combined Std. uncertainty $u_c(\theta)$	—	—	—	—	1.101°	100%
Expanded uncertainty $U_{k=2}$	—	—	—	—	$\pm 2.202^\circ$	—

3. Baseline clearance and optical alignment (u_{d_0}): Mechanical positioning repeatability of the sensor mount introduces an uncertainty of $\Delta d_0 = \pm 0.3$ mm with rectangular distribution:

$$u_{d_0} = \frac{0.3}{\sqrt{3}} \approx 0.173 \text{ mm}. \tag{12}$$

Sensitivity $c_{d_0} = -1.8^\circ/\text{mm}$ gives $u_3 = |c_{d_0}| \cdot u_{d_0} = 0.312^\circ$.

4. Mechanical shaft eccentricity and radial runout (u_{mech}): Dial indicator measurements revealed a peak radial runout of $e_r = 0.15$ mm along the shaft axis. Projected axially onto the helical incline ($\alpha = \arctan(P/\pi D) \approx 12.0^\circ$), this creates a sinusoidal angular deviation of bounds $\pm(e_r \cdot \tan\alpha \cdot c_d) \approx \pm 0.058^\circ$. Assuming a U-shaped distribution for sinusoidal motion:

$$u_4 = u_{mech} = \frac{0.058}{\sqrt{2}} \approx 0.041^\circ \tag{13}$$

5. FDM surface roughness and layer artifacts (u_{surf}): Profilometer inspection of the 3D-printed ABS ramp with 0.1 mm layer height showed an average surface roughness of $R_a \approx 6.0$ μm with peak-to-valley striations bounded by $R_z \approx 0.022$ mm. Local optical scattering resulting from surface micro-geometry causes distance noise bounded by ± 0.022 mm, yielding a rectangular uncertainty contribution:

$$u_5 = u_{surf} = 1.8^\circ/\text{mm} \cdot \frac{0.022}{\sqrt{3}} \approx 0.023^\circ. \tag{14}$$

The combined standard uncertainty is calculated assuming uncorrelated input quantities:

$$u_c(\theta) = \sqrt{u_1^2 + u_2^2 + u_3^2 + u_4^2 + u_5^2} \approx 1.101^\circ. \tag{15}$$

For a coverage factor of $k = 2$ corresponding to an approximate 95% confidence level, the expanded measurement uncertainty U_{95} is:

$$U_{95} = k \cdot u_c(\theta) = \pm 2.202^\circ. \tag{16}$$

This GUM uncertainty budget is summarized in table 2. The budget formally demonstrates that ToF distance sensor quantization u_1 accounting for 88.9% of total variance is the dominant uncertainty contributor. Mechanical and surface roughness effects u_4 and u_5, while present, are an order of magnitude smaller. This confirms that upgrading to a higher-resolution ToF sensor with 0.1 mm resolution would directly reduce U_{95} to sub-degree levels without altering the mechanical geometry.

Figure 8 illustrates the error residuals after calibration and filtering. The error residuals fluctuate evenly around zero within the $\pm 2\sigma$ bounds across all angles, confirming that no unmodeled non-linear trends remain.

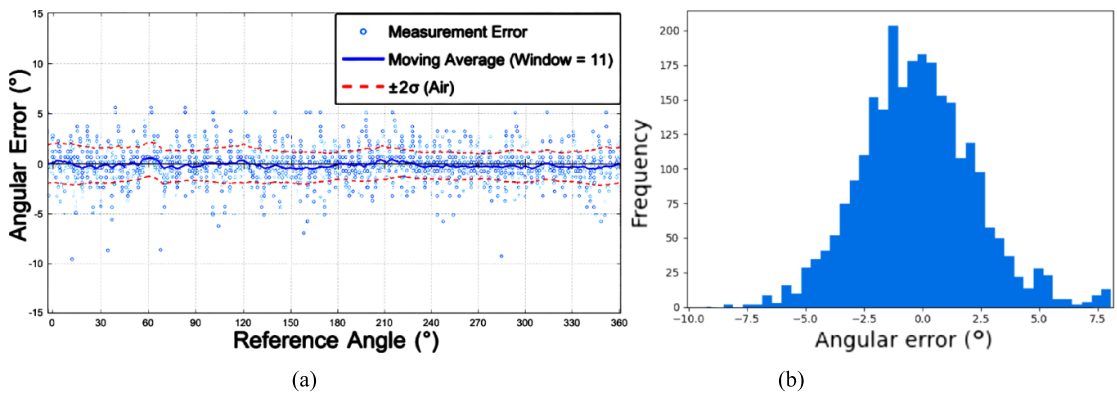

Figure 8. Angular error as a function of reference angle (a) and distribution of angular measurement errors (b) in air after temporal consistency filtering.

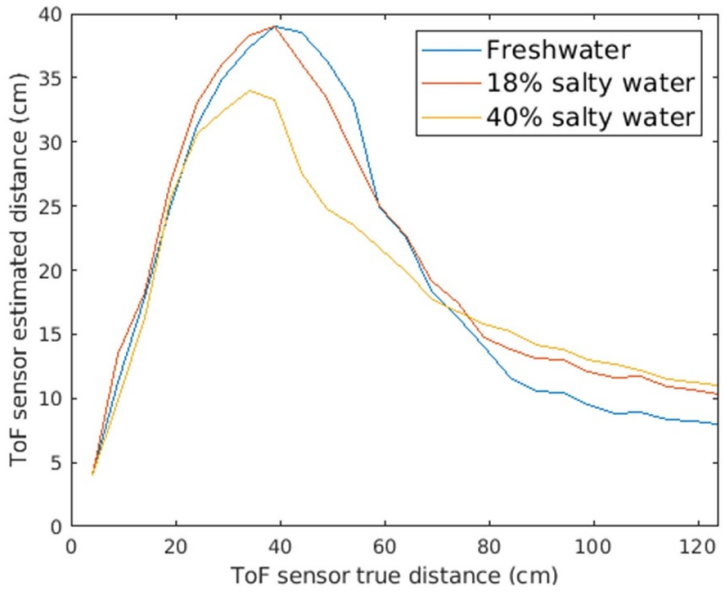

Figure 9. ToF sensor distance estimation vs true distance across various water salinity levels.

4.4. Operation in submerged environments and salinity dependency

To evaluate system performance in submerged environments, absolute angular position estimation was tested at a nominal baseline clearance of 30 cm. To justify this depth limit and establish the operational boundaries of the ToF sensor, explicit ranging capability experiments were conducted in media with varying salinity levels: freshwater, 18 g/l (1.8% salt solution), and 40 g/l (4.0% salt solution). Freshwater represents typical inland lakes and rivers, 1.8% salinity corresponds to low-salinity seas such as the Black Sea, and 4.0% salinity models highly saline marine environments such as the Red Sea and tropical ocean basins, whereas average global ocean salinity ranges between $35-38$ g/l.

Figure 9 presents the estimated ToF distance versus true physical distance across these three salinity regimes. The experimental results reveal that higher salt concentrations increase optical attenuation and turbidity-induced backscattering, which progressively degrades signal-to-noise ratio and reduces the maximum measurable ToF range.

For the low-cost, low-power VCSEL-based ToF sensor utilized in this prototype, the maximum reliable underwater detection range is bounded between 40 cm and 44 cm. Given the helical encoder geometry with a pitch of $P = 200$ mm/rev, this $40-44$ cm operational window seamlessly matches the required physical clearance between the sensor emitter and the uppermost helical target face. Despite the optical speed reduction caused by the refractive index of water (≈1.33), the sensor maintained a linear distance-to-angle relationship within this range. Following empirical calibration $a_{\mathrm{cal}_{\mathrm{water}}} = 2.401°/\mathrm{mm}$, the submerged angular estimation achieved an RMSE of 2.10° with a mean bias of 0.13° (table 1). Figure 10

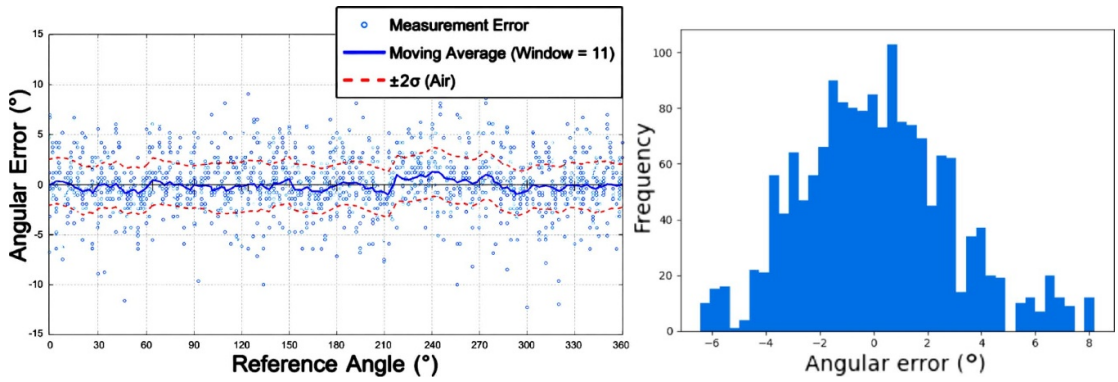

(a) (b)

Figure 10. Angular error as a function of reference angle (a) and distribution of angular measurement errors (b) under submerged conditions after temporal consistency filtering.

demonstrates the residual angular tracking error as a function of the reference angle and the corresponding error distribution histogram under submerged conditions after applying the threshold-based temporal consistency filter. The residual error histogram remains unimodal, centered near zero, and tightly bounded within $\pm 2\sigma$ proving that continuous geometric encoding maintains high measurement stability in liquid media once optical refraction is calibrated.

4.5. Absolute measurement continuity through dead-zone compensation

At the $360° \leftrightarrow 0°$ boundary (figures 1(b), (c) and 2(b), (c)), the helical step creates a dead-zone $\Delta\theta_{\mathrm{dz}} \approx 10°$) where the optical spot $S_{\mathrm{d}} = 22.7$ mm spans both the top and bottom edges. This violates single-point reflection assumptions.

To enable continuous 360° operation, a dual-sensor topology was developed. Two ToF sensors are mounted with a physical spatial offset of $\theta_{\mathrm{offset}} = 90°$. The selection algorithm (figure 11) monitors whether the primary sensor enters the dead-zone threshold $[d_{\min} | d_{\min} + \Delta d_{\mathrm{dz}}]$. When triggered, execution seamlessly switches active reading to the secondary sensor, subtracting the calibrated offset:

$$\theta_{\mathrm{est}} = \theta_{\mathrm{sensor\ 2}} + \theta_{\mathrm{offset}} \pmod{360°} \tag{17}$$

Figure 12 demonstrates complete 360° continuity across forward overflow ($360° \rightarrow 0°$), reverse underflow ($0° \rightarrow 360°$), and direction-reversal regimes. Automated sensor switching eliminates edge anomalies, ensuring uninterrupted absolute tracking across full continuous rotations.

4.6. Dynamic measurement considerations and latency

System dynamic limits were evaluated during continuous rotations, transient stops, and direction reversals with rotational speeds ranging between 14.7 RPM and 100 RPM. The overall end-to-end measurement latency τ_{total} is defined as:

$$\tau_{\mathrm{total}} = \tau_{\mathrm{sensor}} + \tau_{\mathrm{filter}} + \tau_{\mathrm{comm}} \tag{18}$$

where $\tau_{\mathrm{sensor}} \approx 20$ ms due to the $f_{\mathrm{s}} = 50$ Hz sampling rate, $\overline{\tau}_{\mathrm{filter}} \approx 2$ ms is the average algorithmic latency introduced by sample holds with a peak upper bound of $\tau_{\mathrm{filter}_{\max}} = 80$ ms for $N_{\mathrm{hold}_{\max}} = 4$ rejected samples, as detailed in section 4.2 and $\tau_{\mathrm{comm}} \approx 0.478$ ms accounts for RS232 transmission at 230.4 kbps.

During steady rotation at angular velocity ω, this combined latency introduces a dynamic tracking lag $\delta\theta_{\mathrm{dynamic}} = \omega \cdot \tau_{\mathrm{total}}$. As demonstrated by the empirical filter rejection rates $R_{\mathrm{reject}} \approx 4.0\% - 5.2\%$, the system operates without active sample holds for over 94% of sampling intervals, yielding an average latency of $0.1\tau_{\mathrm{s}} = 2.0$ ms. For rotational speeds ranging between 14.7 RPM and 100 RPM, this overall phase delay corresponds to an average angular tracking offset ranging from 0.18°to 1.2°.

Figure 13 demonstrates shaft rotational motion scenarios involving continuous rotation, acceleration transients, 1.5 s dwell stops and direction reversals across the evaluated velocity spectrum. It is observed that the physical phase delay between the ToF sensor estimation and the ground-truth encoder measurement increases linearly with rotational speed.

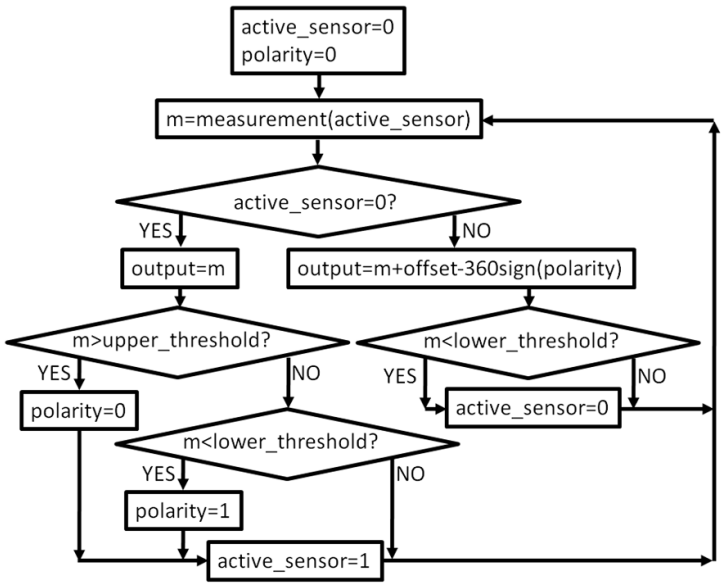

Figure 11. Algorithm schematic of dual sensor dead zone compensation.

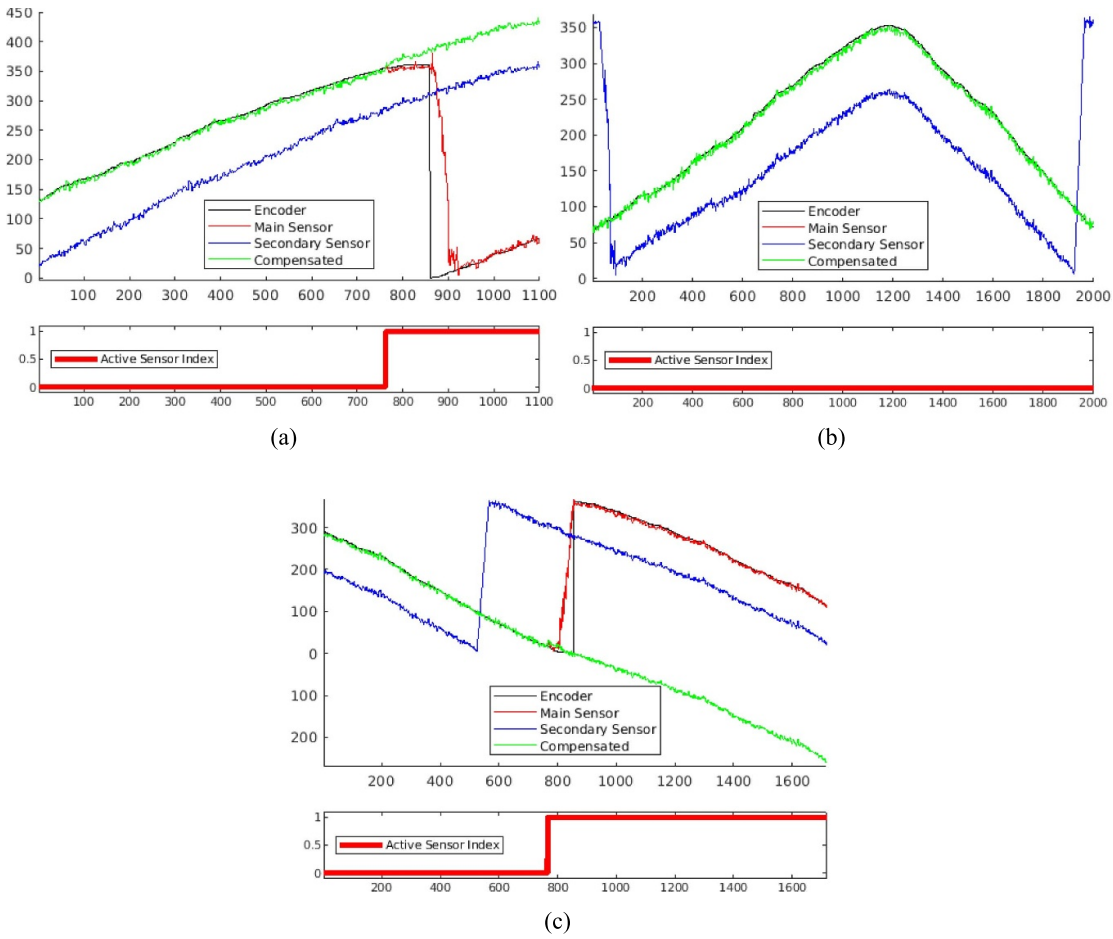

Figure 12. Algorithm performance of dual sensor dead zone compensation in overflow (a), near to overflow (b) and underflow (c) conditions.

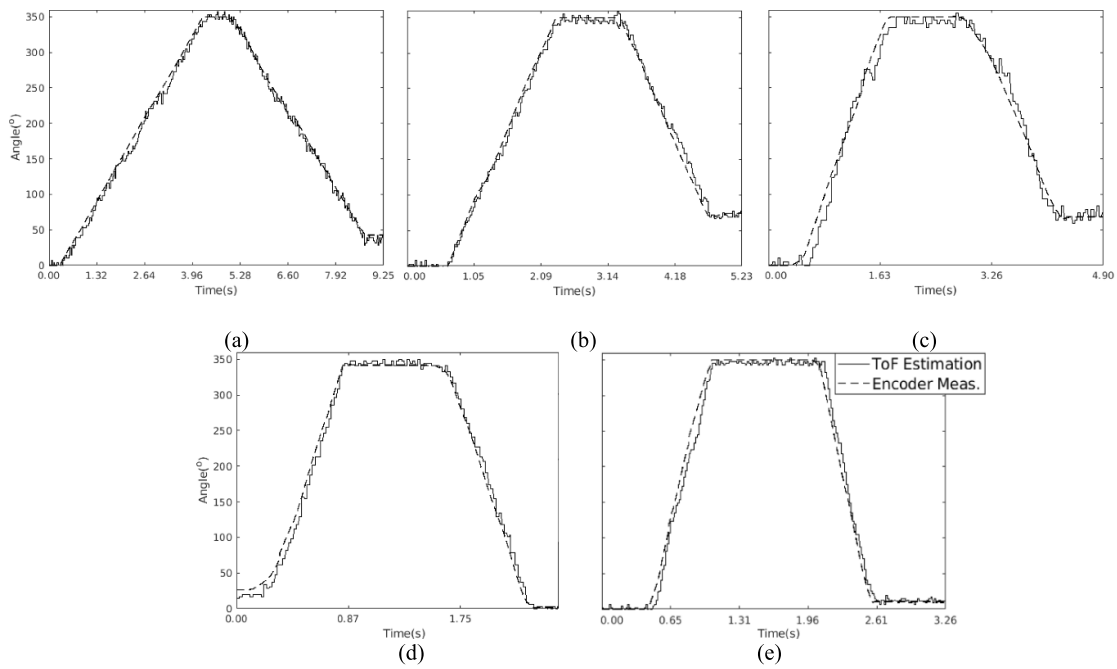

Figure 13. Dynamic measurement performance of the ToF sensor estimation in comparison with ground-truth encoder measurements for 14.7 RPM (a), 35 RPM (b), 50 RPM (c), 90 RPM (d) and 100 RPM (e).

Table 3. Qualitative comparison of the proposed geometric encoding approach with conventional absolute encoders.

Feature	Optical absolute encoder	Magnetic absolute encoder	Proposed geometric encoding
Measurement principle	Coded optical pattern	Magnetic field encoding	Continuous geometric distance encoding
Sensing element	Photodetector array/Image sensor	Hall-effect/ Magnetoresistive array	Single-point ToF distance sensor
Coded reference disk	Required	Required	Not required (Passive helical ramp)
Absolute position recovery	Yes	Yes	Yes
Computational complexity	Low	Low	Low (Single-equation linear mapping)
Submerged capability	Poor (Sensitive to lens fog/particles)	Moderate (Immune to water, sensitive to EMI)	Good (Demonstrated underwater at 10 cm depth)
Scalability with sensor	Required	Fixed by magnetic pole pitch	Directly scales with ToF sensor precision
Sensitivity to EMI	High (Optical paths)	High (Vulnerable to external B-fields)	Very Low (Solid-state VCSEL/SPAD optical)

4.7. Practical considerations and technology comparison

Table 3 presents a qualitative comparison between conventional absolute encoders and the proposed single-point geometric encoding approach.

Unlike traditional absolute encoders that rely on micro-patterned disks or multi-track sensor arrays, the proposed concept relies on a single ranging channel paired with a simple passive helical target. This design prioritizes low cost, mechanical robustness, and environmental adaptability over sub-arcsecond resolution, filling a clear practical niche in moderate-accuracy industrial, robotic, and submerged positioning systems.

5. Conclusion

This study introduced and experimentally validated a continuous geometric encoding principle for absolute angular position measurement. By converting shaft rotation into a monotonic distance variation using a helical reference surface, the proposed system recovers 350° absolute position using a single-point ToF distance sensor.

Key findings and contributions include:

1. Experimental validation: A proof-of-concept prototype built with a VL53L1X ToF sensor demonstrated stable absolute angular estimation in both air (RMSE $= 1.85°$) and shallow submerged conditions (RMSE $= 2.10°$ at 10 cm depth).
2. Impulsive outlier mitigation: The threshold-based temporal consistency filter successfully suppressed stochastic ranging anomalies, reducing raw measurement RMSE by over 95% while maintaining minimal algorithmic latency.
3. Rigorous GUM uncertainty budget: A complete metrological evaluation established an expanded measurement uncertainty ($k = 2$) of $U_{95} = \pm 2.202°$ in air. The analysis proved that sensor distance quantization contributes 88.9% of the total error variance, establishing a clear pathway for sub-degree accuracy by adopting higher-resolution ToF transducers.
4. Continuity and dynamic limits: Dual-sensor dead-zone compensation achieved uninterrupted 360° tracking across wrap-around boundaries. Dynamic evaluations established deterministic latency behavior, enabling velocity-compensated operation during continuous rotations and direction reversals.

Rather than attempting to compete with high-precision optical encoders, the proposed architecture offers a minimal-complexity, low-cost solution tailored for moderate-accuracy robotic joints, industrial grippers, and submerged inspection mechanisms where mechanical simplicity and environmental tolerance are paramount. Future work will explore high-speed micro-LiDAR sensors, optimized metallic helical surfaces, and long-term durability evaluations in dirty and turbid fluids.

Data availability statement

The data cannot be made publicly available upon publication because they are not available in a format that is sufficiently accessible or reusable by other researchers. The data that support the findings of this study are available upon reasonable request from the authors.

Conflict of interest

The author declares no conflict of interest.

Declaration of generative AI and AI-assisted technologies in the writing process

During the preparation of this work, the author used ChatGPT (OpenAI) and Google Gemini in order to improve language clarity and academic writing quality. After using these tools, the author(s) reviewed and edited the content as needed and take full responsibility for the content of the published article.

ORCID iD

Ertugrul Cetinsoy 0000-0001-5398-7409

References

[1] Gao W, Kim S W, Bosse H, Haitjema H, Chen Y L, Lu X D, Knapp W, Weckenmann A, Estler W T and Kunzmann H 2015 Measurement technologies for precision positioning *CIRP Ann.* **64** 773–96
[2] Gao W, Haitjema H, Fang F Z, Leach R K, Cheung C F, Savio E and Linares J M 2019 On-machine and in-process surface metrology for precision manufacturing *CIRP Ann.* **68** 843–66
[3] Engelhardt K and Seitz P 1996 Absolute, high-resolution optical position encoder *Appl. Opt.* **35** 201–8
[4] Wang S, Luo L, Zhu J, Shi N and Li X 2022 An ultra-precision absolute-type multi-degree-of-freedom grating encoder *Sensors* **22** 9047
[5] Wang H, Wang J, Chen B, Xiao P, Chen X, Cai N and Ling B W-K 2015 Absolute optical imaging position encoder *Measurement* **67** 42–50
[6] Das S and Chakraborty B 2018 Design of an absolute shaft encoder using optically modulated binary code *IEEE Sens. J.* **18** 4902–10

[7] Chen Y C, Lee C H, Chou M J and Shen S C 2017 High-precision digital rotary encoder based on dot-matrix gratings *IEEE Photon. J.* **10** 1–12
[8] Zhao M, Yuan Y, Luo L and Li X 2025 A review: absolute linear encoder measurement technology *Sensors* **25** 5997
[9] Denić D, Miljković G, Lukić J and Arsić M 2012 Pseudorandom position encoder with improved zero position adjustment *Facta Univ.-Ser. Electron. Energ.* **25** 113–20
[10] Miljkovic G S and Denic D B 2020 Redundant and flexible pseudorandom optical rotary encoder *Elektron. Elektrotech.* **26** 10–16
[11] Miljković G, Denić D, Pešić M and Arsić M 2013 Improved pseudorandom absolute position encoder with reliable code reading method *Facta Univ.-Ser. Autom. Control Robot.* **12** 121–9
[12] Vocetka M, Huňady R, Hagara M, Bobovský Z, Kot T and Krys V 2020 Influence of the approach direction on the repeatability of an industrial robot *Appl. Sci.* **10** 8714
[13] Chen T, Lin J, Wu D and Wu H 2021 Research of calibration method for industrial robot based on error model of position *Appl. Sci.* **11** 1287
[14] Jia B, Pan H, Cai Y, Zhang L, Chen X and Chen L 2025 Enhancing the absolute positioning accuracy of welding robots based on joint error compensation *Eng. Appl. Artif. Intell.* **158** 111302
[15] Jiang Y, Yu L, Jia H, Zhao H and Xia H 2020 Absolute positioning accuracy improvement in an industrial robot *Sensors* **20** 4354
[16] Niclass C, Favi C, Kluter T, Gersbach M and Charbon E 2008 A 128x128 single-photon image sensor with column-level 10-bit time-to-digital converter array *IEEE J. Solid-State Circuits* **43** 2977–89
[17] Yan S, Tao X and Xu D 2021 High-precision robotic assembly system using three-dimensional vision *Int. J. Adv. Robot. Syst.* **18** 17298814211027029
[18] Pavia J M, Scandini M, Lindner S, Wolf M and Charbon E 2015 A 1× 400 backside-illuminated SPAD sensor with 49.7 ps resolution, 30 pJ/sample TDCs fabricated in 3D CMOS technology for near-infrared optical tomography *IEEE J. Solid-State Circuits* **50** 2406–18